Spread Spectrum Time Domain Reflectometry (SSTDR) Digital Twin Simulation of Photovoltaic Systems for Fault Detection and Location

Samuel R. Kingston[1, *], Cody La Flamme[2], Mashad U. Saleh[1], Hunter Ellis[1], Evan Benoit[1], Ayobami Edun[2], Michael A. Scarpulla[1], Cynthia M. Furse[1, 3], and Joel B. Harley[2]

Abstract—Utilizing spread spectrum time domain reflectometry (SSTDR) to detect, locate, and characterize faults in photovoltaic (PV) systems is examined in this paper. We present a method to obtain the model parameters that are needed to produce digital twin SSTDR responses for PV systems. The digital twin SSTDR responses could be used to predict faults within the PV systems. The model parameters are the reflection and transmission coefficients at each impedance discontinuity in the PV system along with the propagation coefficients across each PV cable segment. We obtain model parameter by applying inverse modeling techniques to experimental SSTDR data associated with PV systems. Our model parameters can be used in any digital twin simulation method for modeling reflectometry in frequency-dependent and complex loads. For validation, we used the model parameters in a graph network simulation engine and adapted it to be used for SSTDR digital twin simulations in PV systems. We produced simulations for 0 to 10 PV modules connected in series. We also simulated SSTDR responses for open circuit disconnections in a PV setup containing 10 PV modules in series. Results show that all but one simulated disconnect locations match experimental disconnection locations of the same setup with an error of less than 5%.

1. INTRODUCTION

Utility photovoltaic (PV) power systems can be significantly degraded by faults, such as open circuits, short circuits, module degradation, ground faults, connection corrosion, shading, etc. [1, 2]. Currently, faults are detected by smart power inverters [3] by comparing the voltage (V), current (I), and power (W) levels to those expected when the system is healthy. Inverters can detect faults in a string or combination of strings but cannot localize it further. Hence, manual troubleshooting is often needed [1]. Reflectometry [4] has been proposed as a method to detect, locate, and characterize faults in PV systems. There are several types of reflectometry, including time domain reflectometry (TDR) [5], frequency domain reflectometry (FDR) [6], joint time-frequency domain reflectometry [7], noise domain reflectometry (NDR) [8], chaos reflectometry [9], sequence time domain reflectometry (STDR) [4], and spread spectrum time domain reflectometry (SSTDR) that have been used in a plethora of system health monitoring applications [10]. While we will focus on the use of spread spectrum time domain reflectometry (SSTDR) for energized PV systems, the work in this paper could be readily adapted to many other reflectometry systems.

One challenge of all reflectometry systems is identifying the fault type and location from the reflectometry signature, particularly when it includes multiple superimposed reflections and

transmissions. This is more complicated if the system includes complex impedances, as in PV systems [11], and/or branched networks [9]. Some algorithms that are used to evaluate the reflectometry signatures associated with faults in branched networks are neural networks [12], particle swarm optimization [13], teaching-learning based optimization [14], inverse scattering [15], and others. For these algorithms, baselining can be used to remove the normal occurring reflections from a healthy system. If an experimental baseline does not exist, an accurate simulated reflectometry response is needed. The methods described in this paper could be used to simulate these baseline responses.

Other reflectometry algorithms use simulations or measurements of faulted conditions to create a dictionary of possible conditions. This dictionary is compared with an unknown measurement to determine which fault type/location is most probable [16–18]. These types of algorithms work best when data can be included for every fault type and location possible. Since this would be difficult to measure, a digital-twin [19–21] simulation that predicts the reflectometry response can be used to replace the experimental data. The accuracy of this digital twin is critical to the effectiveness of the fault location algorithm, and the accuracy of the digital twin is impacted by the accuracy of the model parameters entered into the simulation, such as the characteristic impedance of the transmission line, the reflectometry test device impedance, the PV module's and cable connector's reflection and transmission coefficients, the reflectometry signal's velocity of propagation (VOP), and the effective distance of the PV modules with the connecting cables. It is evident from the literature [6, 19, 20, 22–24] that it is often difficult to identify correct model parameters to produce accurate digital twin simulations. In some applications, a vector-network-analyzer (VNA) or an inductor-capacitance-resistance (LCR) meter is used to measure the frequency-dependent parameters, e.g., the reflection and transmission coefficients. However, a VNA or an LCR meter typically cannot safely measure on energized system with the voltage and/or current above a specific threshold [25–27]. Commercial grade PV modules produce a voltage and current level that is higher than the allowable limit for testing using a VNA or LCR meter. Note also that PV modules cannot be fully "turned off" for testing. Thus, the use of SSTDR to operate on energized systems makes it a great candidate for measuring the frequency dependent parameters for PV modules. In [21], a reflectometry modeling technique was introduced to model reflectometry through full PV modules. However, due to a lack of accurate reflection and transmission coefficient model parameters available, the method was validated with discrete resistors and capacitors. Therefore, there is a need to produce accurate model parameters for PV systems that can be used for fault detection and classification.

The novelty of this paper is our procedure for calculating frequency-dependent model parameters and how they can be used for reflectometry modeling. In addition, we demonstrate how to adapt a simulation engine to emulate PV systems. To validate the accuracy of our model parameters, we used them to produce SSTDR response simulations for $P = 0$ to $P = 10$ PV modules connected in series. We then compared the SSTDR simulations to corresponding experimental SSTDR responses. It is important to note that a reflectometry signal will experience partial energy reflection and transmission at each point where there is a change in impedance. Thus, our measurement of accuracy for our simulations was to evaluate the correlation coefficient, the percent error in the peak location, and the percent error in the peak amplitude of the first three major reflections of the simulated responses compared to the corresponding first three major reflections of the experimental response. In our results, the first and second reflections match well. For further validation, we simulated SSTDR responses for open circuit disconnections in a PV setup containing 10 PV modules in series. When comparing the simulated disconnect locations to experimental disconnect locations of the same setup, all but one simulated disconnect location had an error of less than 5%. Our results demonstrate that our extracted model parameters are sufficiently accurate to model SSTDR propagation through PV modules in series and predict open circuit disconnection locations. Future work will be evaluating the effectiveness of our model parameters in simulating more complex faults.

Section 2 of this paper gives a brief background on SSTDR and defines the full PV system. Section 3 explains our methods of building the model parameters used to construct the digital twin SSTDR response. Section 4 gives a brief description of how we adapt the directional graph network model introduced in [28] to be used in PV systems. Section 5 gives two different sets of validations for our digital twin simulation and compares the simulated results to corresponding experimental data. Section 6 discusses our conclusion and future work.

2. METHODOLOGY: SSTDR DIGITAL TWIN

2.1. Defining the PV System

The test system used in this paper is shown in Fig. 1. The SSTDR test device transmits and receives a PN coded voltage signal differentially across both the positive and negative leads which are connected to a two wire transmission line (PV leader cable) and PV modules, all connected with 4 mm manufacturer multi-contact (MC4) connectors. The SSTDR signal partially reflects at and transmits through each impedance discontinuity/interface [4]. An accurate digital twin response models the superposition of all reflections and the propagation delays through each cable and module. Each interface marked as a vertical blue dashed line produces both a signal reflection and signal transmission. We use blue rebound arrows to indicate a reflection at the interface and a green straight arrow to indicate a transmission. The reflection arrows are only shown on the top lead, and the transmission arrows are shown on the bottom lead for illustrative purposes. The vertical line that goes through both the top and bottom leads is representative of a single interface that exhibits both signal reflection and transmission. Furthermore, each parallel pair of PV modules is modeled as a single interface with a propagation delay (labeled with red θ_s). MC4 connectors are modeled as interfaces with no delay. Each impedance, and therefore each reflection and transmission coefficient, is assumed to be frequency dependent. In the next section, we explain how we experimentally extract the parameters for each component, which will then be combined in simulation to produce the digital twin of the PV system.
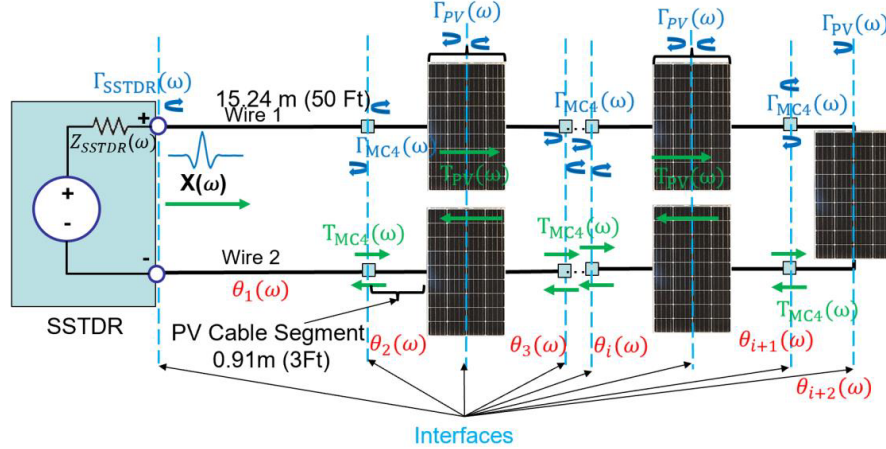
Figure 1. PV system simulation. Impedance discontinuity interfaces are shown as dashed blue lines. The reflection coefficients are labeled with blue rebound arrows, and the transmission coefficients with green directional arrows. Propagation delays are marked with red θ_s. MC4 connectors are shown as small blue boxes, and modules are larger black boxes. A 2-wire transmission line is excited differentially by a voltage source.

2.2. SSTDR Background

In reflectometry, signals are launched from a test device, and the reflections that occur at impedance discontinuities are measured to characterize the system [29]. In spread spectrum time domain reflectometry (SSTDR), the launched signal is a square-wave-modulated pseudo-random noise (PN) code sequence. The reflected signal is cross-correlated with shifted copies of the incident signal to produce the SSTDR response. This contains information about the impedance discontinuities, e.g., distances, complex load impedances, and characterization of faults [4].

For any reflectometry system, including SSTDR, the reflection coefficient $\Gamma(\omega)$ at interfaces between two impedances, Z_1 and Z_2, is a ratio of reflected (V_{ref}) to incident (V_{inc}) signals

$$\Gamma\left(\omega\right) = \frac{V_{\text{ref}}}{V_{\text{inc}}} = \frac{Z_2(\omega) - Z_1(\omega)}{Z_2(\omega) + Z_1(\omega)} \tag{1}$$

The transmission coefficient $T(\omega)$ describes the transmitted signal (V_{trans})

$$T(\omega) = \frac{V_{\text{trans}}}{V_{\text{inc}}} = 1 + \Gamma(\omega) = \frac{2Z_2(\omega)}{Z_2(\omega) + Z_1(\omega)} \tag{2}$$

The SSTDR response shape is dependent on the reflection coefficient value associated with the impedance discontinuities in the system [30]. If Z_2 is an open circuit (OC) (load impedance is infinite Ω), $\Gamma(\omega)$ is equal to $+1$, and the SSTDR response shape is a sinc-like SSTDR response. Conversely, if Z_2 is a short circuit (SC) (load impedance is $0\,\Omega$), $\Gamma(\omega)$ is equal to -1, and the SSTDR response shape is an inverted sinc-like SSTDR response. When Z_2 equals Z_1 (the load is matched to the line), $\Gamma(\omega)$ is equal to 0, and the SSTDR response has no reflection. For resistive loads, the SSTDR sinc-like shape is maintained, but the amplitude ranges from an SC response for smaller impedances to an OC response for larger impedances. Complex loads that contain capacitive or inductive elements introduce a frequency-dependent phase shift to the sinc-like SSTDR response [16, 27].

In this paper, we will find the impedances, and hence reflection and transmission coefficients, for transmission lines, connectors, and PV modules through theoretical analysis and measurement. We will then use these reflection and transmission coefficients to model the complex reflections and transmissions across multiple PV modules connected by transmission lines.

3. BUILDING THE MODEL PARAMETERS

This section explains how we analytically and experimentally extract the model parameters needed to model the SSTDR response of the PV system in Fig. 1. The model parameters are the reflection coefficient at the SSTDR test device $\Gamma_{\text{SSTDR}}(\omega)$, the forward and backward reflection coefficients $\Gamma_{\text{MC4}}(\omega)$ and transmission coefficients $T_{\text{MC4}}(\omega)$ at the MC4 connectors, the forward and backward reflection coefficients $\Gamma_{\text{PV}}(\omega)$ and the transmission coefficients $T_{\text{PV}}(\omega)$ for in-line PV modules, the forward and backward propagation coefficients across each ith PV cable segment $\theta_i(\omega)$, and the reflection coefficient at the end of the transmission line. The reflections at the end of the transmission line can have an open circuit load $\Gamma_{\text{OCend}}(\omega)$, a short circuit load $\Gamma_{\text{SCend}}(\omega)$, or a PV module load $\Gamma_{\text{PVend}}(\omega)$. The accuracy of these reflection and transmission coefficients is critical to the accuracy of the digital twin simulation [31]. This section describes how we obtained these reflection and transmission coefficients.

3.1. Reflection Coefficient at the SSTDR Test Device

In this subsection, we explain how to experimentally extract $\Gamma_{\text{SSTDR}}(\omega)$, the reflection coefficient between the ARNOLD SSTDR test device from LiveWire Innovation [32] and the PV leader cable. The reflection coefficient of the test device is

$$\Gamma_{\text{SSTDR}}(\omega) = \frac{Z_{\text{SSTDR}}(\omega) - Z_0(\omega)}{Z_{\text{SSTDR}}(\omega) + Z_0(\omega)} \tag{3}$$

where $Z_{\text{SSTDR}}(\omega)$ is the impedance of the SSTDR test device, and $Z_0(\omega)$ is the characteristic impedance of the PV cable. We found $Z_{\text{SSTDR}}(\omega)$ to be characterized by a resistance of $68\,\Omega$ in series with a capacitance of $270\,\text{pF}$. We first found the $68\,\Omega$ resistance [32, 33] by connecting a potentiometer directly to the SSTDR box and adjusting it whilst taking SSTDR measurements at each step and noting the potentiometer impedance that produced the minimum reflection response (effectively producing a matched load). We found that $68\,\Omega$ matched best with the test device impedance. We then simulated and measured an SSTDR response for a $15.24\,\text{m}$ ($50\,\text{ft}$) leader cable with an open circuit at the end. When comparing the simulated SSTDR response (with $Z_{\text{SSTDR}}(\omega) = 68\,\Omega$, shown by the green dotted line in Fig. 12(a)) with the experimental SSTDR response (Fig. 12(a) black line), the measured reflection seen at the load had capacitive features that our simulation did not (i.e., the right most peak of the reflection had a greater amplitude than the left most peak [30]). We found that adding a $270\,\text{pF}$ capacitor in series with the 68 ohms for $Z_{\text{SSTDR}}(\omega)$ provided the best match between simulated (blue dashed line in Fig. 12(a)) and experimental responses. Therefore, we set $Z_{\text{SSTDR}}(\omega) = 68\,\Omega + \frac{1}{j\omega}(270\,\text{pF})$, where ω are the angular frequencies in the SSTDR response, for all future simulations.

For our PV strings, the transmission line used was a 10 AWG standard PV system cable with a cross-linked polyethylene (XLPE) insulation. The cable parameters to calculate the theoretical value

Table 1. PV cable parameters [16, 33].

Symbol	Description	Value
d_c	Conductor Diameter	$2.94\,\text{mm}$, $10\,\text{AWG}$
σ_c	Copper Conductance	$5.98 * 10^7\,\text{S/m}$
$\tan\delta_{\text{XLPE}}$	Loss tangent (min, avg, max)	3×10^{-4}, 3.5×10^{-4}, 4×10^{-4}
$\mu_{r_{\text{XLPE}}}$	Relative Magnetic Permeability	0.999994
t_{in}	XLPE insulation thickness	$3.375\,\text{mm}$
D_c	Distance between conductors (min, avg, max)	$0.00675\,\text{m}$, $0.011\,\text{m}$, $0.0153\,\text{m}$
$\varepsilon_{r_{\text{XLPE}}}$	Electric Permittivity (min, avg, max)	2.2, 2.3, 2.4
Z_o	Theoretical Characteristic Impedance (min, avg, max)	$119.1\,\Omega$, $178.5\,\Omega$, $219.5\,\Omega$
VOP	Velocity of Propagation	$0.721 \times$ speed of light

for $Z_0(\omega)$ are given in Table 1. Using these theoretical parameters and a twin-lead RLGC model [29], the range of possible $Z_0(\omega)$ was determined to be from $119.1\,\Omega$ to $219.5\,\Omega$. The twin-lead model was chosen since the PV leader cable was two cables taped together and resembled a twin-lead transmission line. The distance between the conductors D_c is defined in Table 1. Both conductors that are taped together have the same length.

Given the expected uncertainty in the theoretical values for $Z_0(\omega)$, we next measured $Z_0(\omega)$. We first measured the SSTDR response of a $15.24\,\text{m}$ ($50\,\text{ft}$) PV leader cable with an open circuit load. The peak value at the open circuit represents a reflection coefficient of 1 (the maximum reflection coefficient possible) and is used to normalize all other measurements. We then measured the SSTDR response of the PV cable connected to a resistive load of $Z_L = 295\,\Omega$. Fig. 2 shows the normalized SSTDR responses for both measurements. We up-sampled the SSTDR response by a factor of 10 for both measurements using spline interpolation [33] and normalized the amplitudes by dividing both data sets by the maximum value in the open circuit data, giving

$$\Gamma_{\text{res}}(\omega) = \frac{\text{Res}_{\text{peak}}}{\text{OC}_{\text{peak}}} = \frac{0.2855}{0.7401} = 0.3887. \tag{4}$$

Then the characteristic impedance $Z_0(\omega)$ is found from Eq. (1):

$$Z_0(\omega) = \frac{Z_L(1 - \Gamma_{\text{res}})}{(1 + \Gamma_{\text{res}})} = \frac{295(1 - 0.3887)}{(1 + 0.3887)} \approx 130\,\Omega. \tag{5}$$

The value of $Z_0(\omega)$ was determined to be weakly frequency dependent with approximately 0.03% change across the entire frequency bandwidth of the SSTDR signal [34]. For simplicity we modeled $Z_0(\omega)$ to be the same across all frequencies. This is the value used for all future simulations.
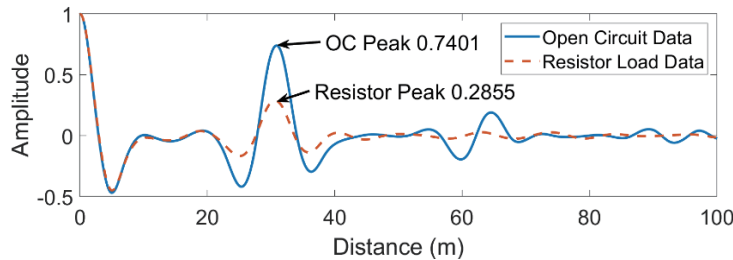
Figure 2. SSTDR response data used to measure Z_0. The open circuit data is solid, and the resistor data is dashed.

3.2. Propagation Coefficients for PV Cable

Each transmission line segment in Fig. 1 is represented by the transmission line's complex propagation coefficient $\gamma(\omega)$, which is defined according to the classic RLGC model for a transmission line [29]

$$\gamma(\omega) = \sqrt{(R + j\omega L)(j\omega C + G)} \tag{6}$$

The parameters used to obtain the RLGC values for the PV cable are found from its twin-lead model, as described in Table 1, and substituted into the twin-lead RLGC model equations in [29]. The imaginary part of the propagation coefficient defines the frequency-dependent phase delay, and the real part defines the frequency-dependent attenuation. The frequency dependent propagation delay for each transmission line segment in Fig. 1 is defined by

$$\theta(\omega) = e^{-\gamma(\omega)(\Delta d)}. \tag{7}$$

where Δd is the length of each respective segment. For the leader cable segment, Δd is 15.24 m (50 ft), from physically measuring the cable. For the PV module and connecting cables segment, Δd is calculated in Subsection 3.7 of this section.

3.3. Reflection and Transmission Coefficients at MC4 Connectors or Damaged Wiring

In this subsection, we explain how to experimentally extract the reflection and transmission coefficients, $\Gamma_{\mathrm{MC4}}(\omega)$ and $T_{\mathrm{MC4}}(\omega)$, for the MC4 connectors or partially damaged wiring. We consider three conditions: a well-connected MC4 connector or wire, a disconnected connector or broken wire, and a partially disconnected connector (such as from corrosion) or partially damaged wire. When the MC4 connector or wire is in good condition and properly connected (Fig. 3(a)), our experimental SSTDR measurements showed that the reflections were extremely small. Thus, we model its impedance as an ideal connection with full transmission ($T_{\mathrm{MC4}}(\omega) \approx 1$) and no reflection ($\Gamma_{\mathrm{MC4}}(\omega) \approx 0$) at all frequencies.
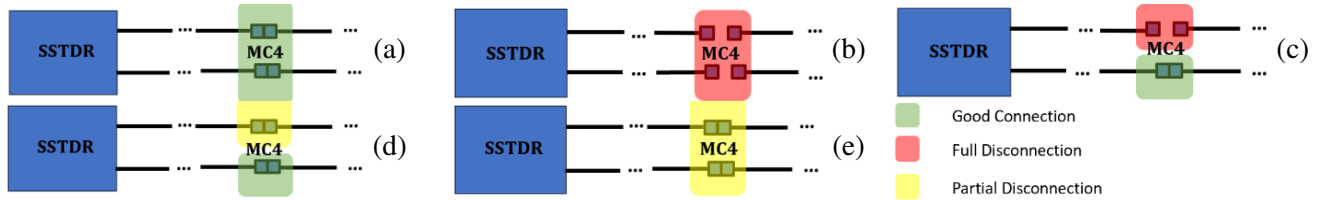
Figure 3. MC4 or cable connection/disconnection scenarios. (a) is for good connection on both lines, (b) is for full disconnection on both lines, (c) is full disconnection on one line and good connection on second line, (d) is a partial disconnection on one line and a good connection on second line, (e) is a partial disconnection on both lines.

If an MC4 connector is disconnected, or a wire is broken (Fig. 3(b) or Fig. 3(c)), our experimental SSTDR measurements showed a full reflection. Thus, we model the connection as an open circuit with $\Gamma_{\mathrm{MC4}}(\omega) = 1$ and $T_{\mathrm{MC4}}(\omega) = 0$ for all frequencies. When there is a partial disconnection, such as from corrosion, on one of the two lines (Fig. 3(d)), we model the connection as an asymmetric frequency-dependent in-line impedance $Z_i(\omega)$ with reflection coefficient [35]

$$\Gamma_{\mathrm{MC4\,Asym}}(\omega) = \frac{Z_i(\omega)}{Z_i(\omega) + 2Z_0(\omega)} \tag{8a}$$

and the transmission coefficient [35]

$$T_{\mathrm{MC4\,Asym}}(\omega) = \frac{2Z_0(\omega)}{Z_i(\omega) + 2Z_0(\omega)} \tag{9a}$$

where $Z_0(\omega) = 130\,\Omega$ is the characteristic impedance of the PV cable. When there is a symmetric partial disconnection (Fig. 3(e)), we can model the connection as a symmetric frequency-dependent

in-line impedance $Z_i(\omega)$ with reflection coefficient [35]

$$\Gamma_{\text{MC4 Sym}}(\omega) = \frac{Z_i(\omega)}{Z_i(\omega) + Z_0(\omega)} \qquad (8b)$$

and the transmission coefficient [35]

$$T_{\text{MC4 Sym}}(\omega) = \frac{Z_0(\omega)}{Z_i(\omega) + Z_0(\omega)} \qquad (9b)$$

The symmetric and asymmetric reflection and transmission coefficient just described were tested experimentally using series connected resistors and capacitors in [35]. To model the in-line impedance of the damage $Z_i(\omega)$ we used experimental SSTDR measurements of partially damaged PV cable shown in Fig. 4. Damage was created with a single razor cut (Fig. 4(a)), progressing until all the conductor strands are cut but are held together to maintain some electrical contact (Fig. 4(h)).

    (a)   (b)   (c)   (d)   (e)   (f)   (g)   (h)
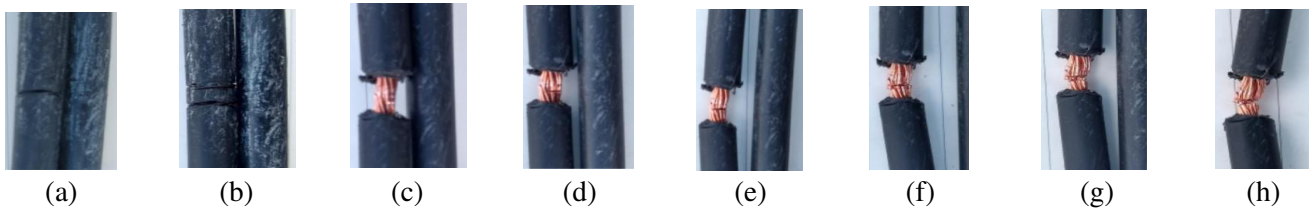
Figure 4. Cable with incremental damage SSTDR measurements were taken for each of the cases (a) through (h).

SSTDR measurements were taken for each scenario in Figs. 4(a) through (h). The SSTDR was connected to $42.44\,\text{m}$ ($139.25\,\text{Ft}$) of 10 AWG multiconductor cross-linked polyethylene (XLPE) type PV cable with the damage from Fig. 4 induced in-line at $35.36\,\text{m}$ ($116\,\text{Ft}$) and five $100\,\text{W}$ Renogy PV modules connected at the end of the cable. The reflection coefficients, shown in Fig. 5, were calculated by dividing the peak of the reflection at the inserted fault by the peak of the reflection of an open circuit at the same location (as in the calculation for Z_0). We can compare these reflection coefficients to those obtained for series connected impedances. For simplicity of measurements and calculation, we chose to have our inserted impedances be resistors with respective resistances of $5\,\Omega$, $10\,\Omega$, and $20\,\Omega$. Thus, we model $Z_i(\omega)$ as being purely real. The corresponding reflection coefficients values are shown as horizontal dashed lines on Fig. 5. The bulk of the reflection coefficients for the partial disconnections (a) through (h) lies in the range of the reflection coefficient for the $5\,\Omega$ to $10\,\Omega$ series resistances.
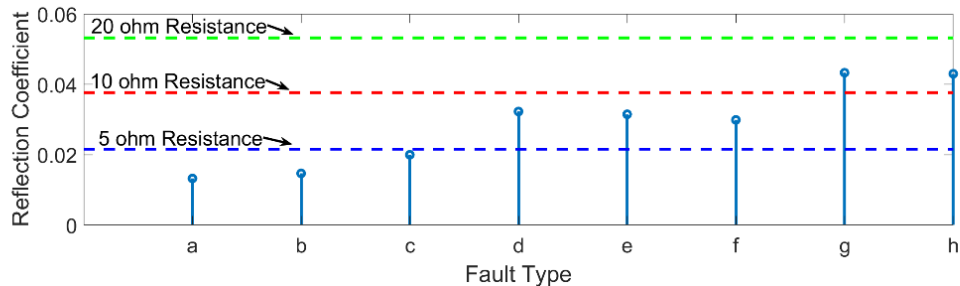
Figure 5. Reflection coefficients from all measured partial disconnects compared to reflection coefficients from resistances. Measured partial disconnects are comparable to resistances of 5 to 10 Ohms.

These results enable us to model partial disconnections as in-line impedances $Z_i(\omega)$. For the average of the series resistance $Z_i(\omega) \approx 7.5\,\Omega$, the associated reflection coefficient from Eq. (8a) is 0.028, and the transmission coefficient from Eq. (9a) is 0.972. For a similar $7.5\,\Omega$ symmetric fault (Fig. 3(e)), the

reflection coefficient from Eq. (8b) is 0.055, and the transmission coefficient from Eq. (9b) is 0.945. Note that these values can be used to model the impedance of either an MC4 connector or damage in the wiring.

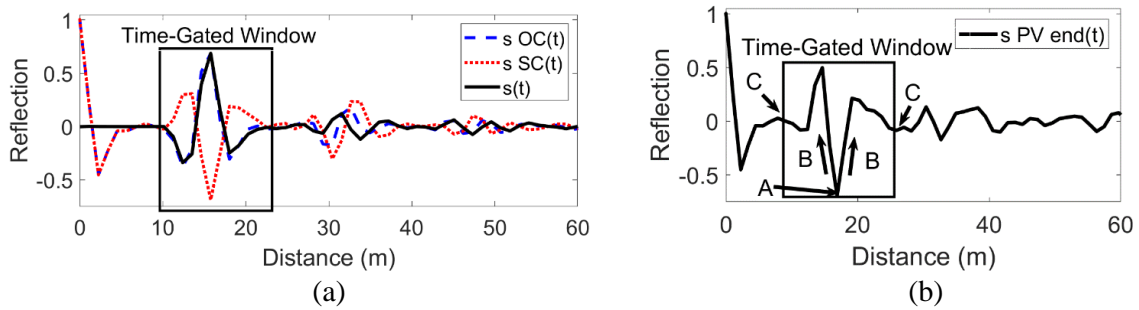### 3.4. Reflection Coefficient for PV Module Load

The PV system in Fig. 1 has two configurations. In this subsection, we will discuss the configuration in which there is a PV module at the end of the line (at the load) and how to experimentally extract $\Gamma_{\text{PVend}}(\omega)$, its reflection coefficient. Currently, there exists a method for estimating the impedance of a PV module in [31] based on the analytical impedance model of individual solar cells from [36]. For a small number of solar cells connected in series, the analytical impedance model of cells gives accurate impedances and accurate SSTDR responses [37]. However, for 60-cell PV modules, the simulations did not match with experimental data. The disparity in the simulation and experimental responses is likely due to other components within the PV module that are not explicitly modelled (e.g., junction box, bypass diodes, bus bars, encapsulant on the top and bottom of the solar cells, the back sheet, glass, and surrounding frame) [38]. Modeling all these individually would be difficult. Therefore, we instead experimentally extract the reflection and transmission coefficient from measured SSTDR data.

The reflection coefficient $\Gamma_{\text{PVend}}(\omega)$ is extracted from measurements of a transmission line terminated by an open circuit (OC), a short circuit (SC), and the PV module, as shown in Fig. 6. The time-domain responses of the OC and SC are shown in Fig. 7(a) and the response with the PV module in Fig. 7(b). We normalize each signal by dividing by the maximum value (located at distance = 0 m) in the open circuit response $s_{\text{OC}}(t)$ (blue dashed line in Fig. 7(a)). We then remove the reflection between the SSTDR and cable (at time $t = 0$) and isolate the SSTDR signal at the load by computing

$$s(t) = \frac{s_{\text{OC}}(t) - s_{\text{SC}}(t)}{2}, \tag{10}$$
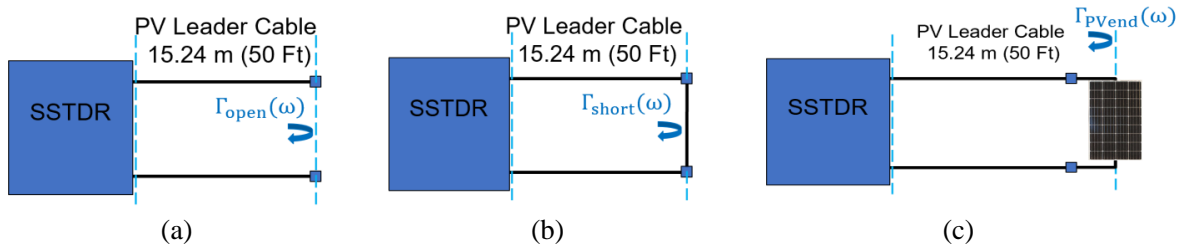
Figure 6. Experimental setups used to extract the reflection coefficient for an end-terminated module. (a) Open circuit load, (b) short circuit load, and end-terminated module load.

Figure 7. (a) SSTDR response for OC data $s_{\text{OC}}(t)$ (blue dashed), SC data $s_{\text{SC}}(t)$ (red dotted), and incident signal $s(t)$ (black solid). Also shows time gated window for $s(t)$. (b) SSTDR response to calculate end module reflection coefficient which is the data for end connected module $s_{\text{PVend}}(t)$ with time gate window and letters A, B, and C to illustrate how the time gate window is identified.

where $s_{OC}(t)$ (blue dashed line in Fig. 7(a)) is the OC response (including the reflection at the SSTDR), and $s_{SC}(t)$ (red dotted line) is the short circuit response (also including the reflection at the SSTDR). The signal $s(t)$ from Eq. (10) removes the reflection at the SSTDR and retains the shape and magnitude of the SSTDR response at the OC/SC location. This includes any frequency-dependent attenuation or dispersion that occurs in the cable. We will use this signature as the incident signal $s(t)$ in our simulation model. The leader cable is included in the measurement to retain the complete reflection signature from the PV module. Without the PV leader cable, the reflection signature from the PV module would experience interference from the reflection response at the SSTDR test device.

Next, the SSTDR reflection with a PV module load $s_{PVend}(t)$, shown in Fig. 6(c), is measured, and the results are shown in Fig. 7(b). We then time gate [39] both $s(t)$ and $s_{PVend}(t)$ to isolate the portion of the signal that encodes the impedance at the end of the cable. The time gate window (the box shown in Fig. 7(b)) can be selected several ways. A Hilbert transform was used in [21], but we will select a computationally simpler strategy. We determine the time gate window by identifying the point of the reflection with the greatest magnitude (marked "A" in Fig. 7(b)). Then we expand the window in the left and right directions until the derivative of the data switches signs twice (marked "B" in Fig. 7(b)). We continue to expand the window until the data reaches a value equal to the average of the signal $+/-0.01$ (marked "C" in Fig. 7(b)).

The time gated responses for both $s(t)$ and $s_{PVend}(t)$ were then shifted so that their "center of mass" is at time $= 0$, or distance $= 0$ meters. We define the center of mass c as

$$c = \frac{\sum_{i=1}^{N-1} i\,|x(t_i)|}{\sum_{i=1}^{N-1} |x(t_i)|} \tag{11}$$

where $x(t_i)$ is a generalized expression to define the amplitude of the measured signal at the ith time sample index; i is the sample index; and N is the number of samples in the measured signal. We refer to this as the "center of mass" as it is the same expression used to calculate the center of a mass distribution. It can also be considered an expected value, where the absolute value of the signal is a probability distribution. By shifting the signal, we remove propagation delays and minimize the frequency-domain phase.

The reflection coefficient $\Gamma_{PVend}(\omega)$ is then calculated using division in frequency (deconvolution in time) as

$$\Gamma_{PVend}(\omega) = \frac{S_{PVend}(\omega)}{S(\omega) + \sigma} \tag{12}$$

where $S(\omega)$ and $S_{PVend}(\omega)$ are computed by converting the time gated and shifted responses of $s(t)$ and $s_{PVend}(t)$ to the frequency domain by applying the Fourier transform. The regularization factor $\sigma = 0.202$ was added in the denominator to prevent the possible division by zero (or close to zero) for all frequencies in the SSTDR response. The σ value is approximately one tenth of the maximum amplitude of $S(\omega)$. The value $\sigma = 0.202$ was found empirically to provide the best match validation between simulated and measured results, which we explain in more detail in Section 5. If σ is too low, the simulated data has high frequency ringing. If σ is too high, the simulation is strongly attenuated. The resulting reflection coefficient is directly in our future simulations, and the impedance can be extracted from Eq. (5). The data signals Fig. 7(a) and Fig. 7(b) are the true signals that that are received and processed using the SSTDR test device. We chose to leave the sampling rate the same and not up-sample them so that we would not introduce approximation error in the newly added sample points which would translate to error in the respective frequency response points in the calculated reflection coefficient. In Section 4, the results and validation, we up-sampled the digital twin SSTDR response data only after the signal was built first using the true SSTDR sampling rate for each of the respective parameters that are needed to build the digital twin.

3.5. Reflection Coefficients for In-Line PV Modules

In this subsection, we explain how to experimentally extract the reflection coefficient $\Gamma_{PV}(\omega)$ for a pair of parallel in-line PV modules by isolating the reflection from a single module pair. In theory, this
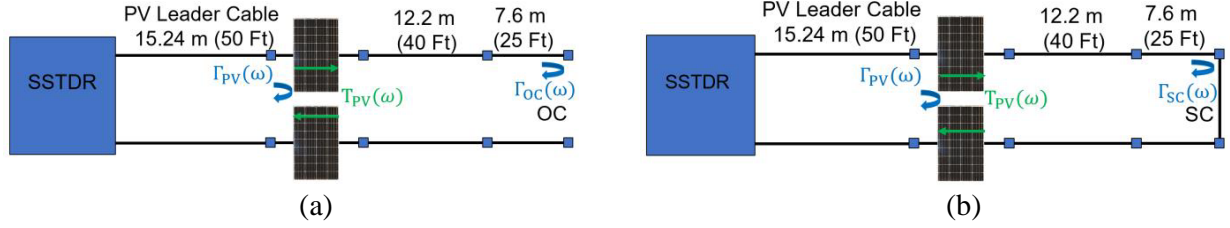
Figure 8. Experimental setups used to extract the in-line reflection, transmission, and propagation coefficients. The data sets are (a) $S2_{\mathrm{OC}}(t)$, and (b) $S2_{\mathrm{SC}}(t)$.
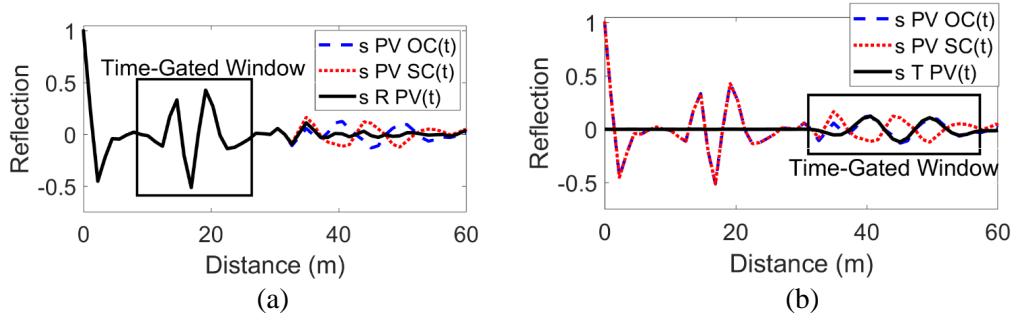

Figure 9. (a) SSTDR response to measure in-line reflection coefficient which includes data for in-line connected modules with OC end (blue dashed), SC end (red dotted), and isolated module reflection (black solid) with time gate window illustrated. (b) SSTDR response to measure in-line transmission coefficient which includes data for in-line connected modules with OC end (blue dashed), SC end (red dotted), and isolated module transmission (black solid) with time gate window illustrated.

could be accomplished by terminating the transmission line with a matched load and time gating to evaluate the reflection from the module pair. However, we performed a simple set of experiments for an OC end and SC end to extract both the reflection and transmission coefficient (from Subsection 3.6) from roughly the same experimental setup. Specifically, we find $\Gamma_{\mathrm{PV}}(\omega)$ from two SSTDR experiments, shown in Fig. 8 with SSTDR responses shown in Fig. 9(a), to remove signals that transmit through the panels and isolate signals that reflect from the panels. For both Fig. 8 and Fig. 10, the cables (15.24 m, 12.2 m, and 7.6 m) are two 10 AWG cables taped together to resemble a twin-lead transmission line. The distance between the cables D_c is 0.011 m as described in Table 1.

Similar to Eq. (13), we remove the transmitted components by adding the open-circuit $s_{\mathrm{PVOC}}(t)$ (shown as a blue dashed line in Fig. 9) and short-circuit $s_{\mathrm{PVSC}}(t)$ (shown as a red dotted line in Fig. 9) responses and dividing by 2 to get $s_{\mathrm{RPV}}(t)$ (shown as black solid line in Fig. 9(a)), defined by

$$s_{\mathrm{RPV}}(t) = \frac{s_{\mathrm{PVOC}}(t) + s_{\mathrm{PVSC}}(t)}{2}. \tag{13}$$
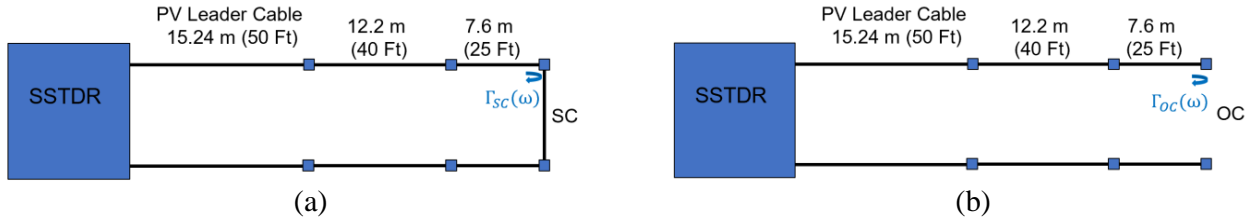
Figure 10. Experimental setups with no PV modules which are compared to setups with modules to measure the effective distance Δd through the PV modules.

This removes transmitted components that reflect at the OC/SC loads, since the short-circuit and open circuit have equal and opposite reflection coefficients. The reflections from the solar panels remain unchanged in the two signals. We then time gate $s_{\mathrm{RPV}}(t)$ in the same manner described in Subsection 3.4 and convert the time gated and shifted signal into the frequency domain $S_{\mathrm{RPV}}(\omega)$ with the Fourier transform. The in-line module reflection coefficient is then computed as

$$\Gamma_{\mathrm{PV}}(\omega) = \frac{S_{\mathrm{RPV}}(\omega)}{S(\omega) + \sigma} \tag{14}$$

where $S(\omega)$ and σ are the same as in Eq. (15).

3.6. Transmission Coefficients for In-Line PV Modules

In this subsection, we explain how to experimentally extract the transmission coefficient $T_{\mathrm{PV}}(\omega)$ for a pair of in-line PV modules. Like finding the in-line reflection coefficient $\Gamma_{\mathrm{PV}}(\omega)$, we find $T_{\mathrm{PV}}(\omega)$ by collecting the SSTDR reflection responses from the setups shown in Fig. 8. However, the goal is to now isolate signals that transmit through the modules $s_{\mathrm{TPV}}(t)$. Therefore, we subtract $s_{\mathrm{PVSC}}(t)$ (shown as a red dotted line in Fig. 9) from $s_{\mathrm{PVOC}}(t)$ (shown as a blue dashed line in Fig. 9) and divide by 2 to get $s_{\mathrm{TPV}}(t)$ (shown as the black solid line in Fig. 9(b)) as

$$s_{\mathrm{TPV}}(t) = \frac{s_{\mathrm{PVOC}}(t) - s_{\mathrm{PVSC}}(t)}{2}. \tag{15}$$

The subtraction removes reflections from the panels and isolates signals transmitted through the panels. We then time gate $s_{\mathrm{TPV}}(t)$ in the same manner as described in Subsection 3.4 and convert the time gated and shifted signal into the frequency domain $S_{\mathrm{TPV}}(\omega)$ with the Fourier transform. The transmission coefficient $T_{\mathrm{PV}}(\omega)$ is then calculated as

$$T_{\mathrm{PV}}(\omega) = \sqrt{\frac{S_{\mathrm{TPV}}(\omega)}{S(\omega) + \sigma}}, \tag{16}$$

where $S(\omega)$ and σ are the same as in Eqs. (12) and (14). We apply the square root in the solution to account for the SSTDR signal transmitting through the modules twice (forward and backward). The transmission coefficient is assumed to be the same for waves traveling in both the forward and reverse directions. Similar to the data shown in Fig. 7(a) and Fig. 7(b), we chose to leave the sampling rate for the data shown in Fig. 9(a) and Fig. 9(b) to be the true sampling rate of the collected SSTDR data (96 MHz) for more accurate parameters that would not add approximation error in the transmission coefficient.

3.7. Propagation Coefficients for In-Line PV Modules

In this subsection, we explain how to experimentally extract the propagation coefficient for a pair of in-line PV modules. Unlike a resistor, capacitor, or small number of solar cells, a PV module cannot be modeled as infinitesimally small interface in the transmission line. Therefore, we must identify the effective electrical length of the module Δd_{PV}. We do this by finding the time difference between SSTDR signals with and without the PV modules in the transmission line and converting that to distance using the average velocity of propagation (VoP). Fig. 10 illustrates the transmission line without PV modules, and Fig. 8 illustrates the transmission line with PV modules. For both scenarios, we isolate the signals that transmit through the transmission line by taking measurements with both an open and a short circuits, added and divided by 2. The resulting data with the PV modules $s_{\mathrm{TPV}}(t)$ and without the PV modules $s_T(t)$ are shown in Fig. 11. The time difference is computed by determining the center of mass of $s_T(t)$ and $s_{\mathrm{TPV}}(t)$ and computing their difference $\Delta d_{\mathrm{PV+cables}} \approx 10.14\,\mathrm{m}$ (33.26 ft). This is the effective length of the PV module plus its built-in cabling. Starting with this value, we manually adjusted this length in the simulation and found empirically that $\Delta d_{\mathrm{PV+cables}} \approx 11.47\,\mathrm{m}$ (37.64 ft) gave the best match with experimental data. Furthermore, by separating $\Delta d_{\mathrm{PV+cables}} \approx 11.47\,\mathrm{m}$ (37.64 ft) into $\Delta d_{\mathrm{PV}} = 6.72\,\mathrm{m}$ (22.04 ft) and $\Delta d_{\mathrm{cables}} \sim 2.37\,\mathrm{m}$ (7.8 ft), which is added to the other cable lengths, we empirically found the best comparison between simulations and measurements. This difference
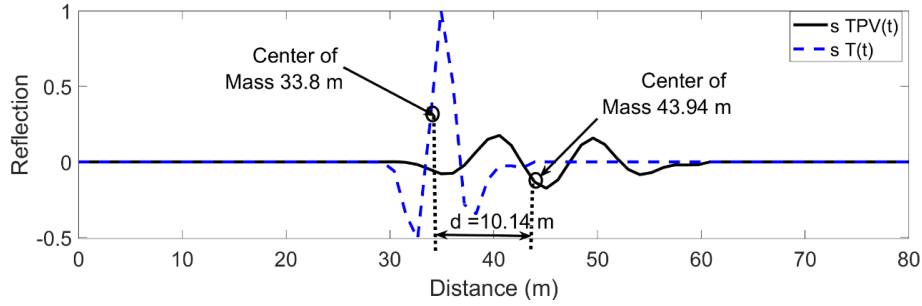
Figure 11. SSTDR response data to measure effective length of modules with connected cables, which includes the response for no modules (blue dashed) and the response with modules (black solid) and the associated center of mass for the data and the difference.

$(1.34\,\text{m}\,(4.38\,\text{ft}))$ could arise from a few sources, such as the limited sampling rate of the SSTDR signal or the fact that the center of mass may be an imperfect measure of propagation time.

The propagation (phase) delay through the PV modules is then added to the transmission coefficient as

$$T_{\text{PV+Delay}}(\omega) = T_{\text{PV}}(\omega)\, e^{-\frac{j\omega \Delta d_{\text{PV+cables}}}{\text{VoP}}} \tag{17}$$

where VoP is the velocity of propagation (m/s) of the SSTDR signal through the PV modules and connecting cables. The distance $\Delta d_{\text{PV+cables}}$ is the calculated effective length given the time delay for the incident signal to arrive back to the SSTDR test device and a chosen VoP of the signal. For the VoP, we chose to use the measured VoP [33] through a PV cable of $0.721c$ where $c \approx 3 \times 10^8\,\text{m/s}$ (the speed of light in a vacuum). Since we are measuring the effective length and not necessarily the true length, we can use the same VoP for the PV modules and the connecting cables.

4. SIMULATING THE FULL SYSTEM

The previous section explained how to extract frequency-dependent reflection coefficients, transmission coefficients, and propagation coefficients associated with each interface in a PV system, namely $\Gamma_{\text{SSTDR}}(\omega)$, $\Gamma_{\text{MC4}}(\omega)$, $T_{\text{MC4}}(\omega)$, $\Gamma_{\text{PVend}}(\omega)$, $\Gamma_{\text{PV}}(\omega)$, $T_{\text{PV}}(\omega)$, $\theta_i(\omega)$, $\Gamma_{\text{SC}}(\omega)$, and $\Gamma_{\text{OC}}(\omega)$. It is important to note that the light intensity/illumination does affect the impedance slightly as demonstrated in [17] where there was a change in the SSTDR responses associated with day and night measurements. Thus, for the best accuracy, the model parameters should be extracted from PV modules that have similar light intensity/illumination to the PV systems in the field being evaluated. In this section, we briefly describe our method to simulate a digital twin SSTDR response through a PV system by incorporating these model parameters into a fast graph network simulation technique [28] that can emulate one-dimensional wave propagation through multi-segment transmission lines. Our simulations were produced using Matlab 2018^{TM}.

We will summarize the simulation engine here. Additional details are in [28]. The engine models a transmission line as a graph. In the graph, the nodes represent frequency domain voltages, and the weights for the edges/connections in the graph are transfer functions, i.e., our calculated model parameters. To produce a simulation, we compute the infinite sum of multiplications between powers of the graph's adjacency matrix $\mathbf{A}$ and initial voltage conditions vector $\mathbf{v}^{(0)}$ for each node within the graph network. This is expressed as

$$\mathbf{V}(\omega) = \sum_{k=1}^{\infty} \mathbf{A}^i(\omega)\, \mathbf{v}^{(0)}(\omega) \tag{18}$$

The infinite sum is then simplified using the Neumann series and matrix inverse as in [28]

$$\mathbf{V}(\omega) = [\mathbf{I} - \mathbf{A}(\omega)]^{-1}\, \mathbf{v}^{(0)}(\omega) \tag{19}$$

where $\mathbf{I}$ is the identity matrix. $\mathbf{V}(\omega)$ contains the frequency response of the superposition of all voltages reaching every node within the graph. The frequency response is made up of Q frequency bins from the fast Fourier transform of the SSTDR response and is dependent on the SSTDR modulation frequency f_m and the sampling frequency f_s. The initial condition vector $\mathbf{v}^{(0)}(\omega)$ only contains values at one node, representing the SSTDR device. For this paper, the initial conditions across frequency are modeled after the output of an Arnold SSTDR device from LiveWire Innovation, which transmits a PN code where the chip rate and the modulation frequency $f_m = 24\,\text{MHz}$, and the sampling rate f_s is $96\,\text{MHz}$ ($4f_m$) [21]. Therefore, the frequency range of the SSTDR is from $-48\,\text{MHz}$ to $+48\,\text{MHz}$. We use a 1,024-point FFT, which makes our frequency resolution $\Delta f = (2)(48\,\text{MHz})/1,204 = 46.87\,\text{kHz}$.

After $\mathbf{V}(\omega)$ is calculated for these Q frequencies, the time domain response $\mathbf{V}(t)$ is computed from the column wise inverse fast Fourier transform of $\mathbf{V}(\omega)$. The columns of $\mathbf{V}(t)$ contain the SSTDR time domain responses arriving at the nodes. Since both node 1 and node $N/2 + 1$ are located at the SSTDR device, the final SSTDR time domain response is calculated by adding the column 1 data with the column $N/2 + 1$ data in $\mathbf{V}(t)$. We validated our model parameters using this graph network technique because of its computational efficiency and ability to model reflectometry through frequency-dependent loads. Note that our model parameters could be used in any simulation engine that is able to model reflectometry through frequency-dependent loads, e.g., finite difference time domain (FDTD) [40], ((FD)^{2}TD) [41], and the systematic solution procedure (SSP) [21]. In the next section, we validate our digital twin SSTDR response by comparing the SSTDR simulations to experimental SSTDR responses for various PV setups. These methods could also be adapted for other types of reflectometry signatures.

5. VALIDATION AND RESULTS

In this section, we validate our digital twin by evaluating the SSTDR responses for P connected modules in series (for $P = 0$ to 10) and for disconnections of the MC4 connectors between them. Our real measurements were taken using an ARNOLD SSTDR test device from LiveWire Innovation [32] set to a $24\,\text{MHz}$ modulation frequency. The PV cables used are characterized using the parameters in Table 1. For the PV modules, we used 60-cell modules with parameters described in [37].

5.1. SSTDR Response Validation for PV Modules Connected in Series

First, we validate the SSTDR response simulation versus experimental SSTDR responses for PV modules connected in series. The experimental setup is shown in Fig. 1 for P modules. The simulated and experimental SSTDR responses are shown in Fig. 12(a) through (h) for $P = 0, 1, 2, 3, 4, 6, 8, 10$, respectively. The validation was done separately for each of the three main time gated reflections (labeled "r1", "r2", and "r3" in Fig. 12). The time gate window was determined for the first reflection, as described in Section 3. The second and third reflection windows were identified by using the same gate width and setting the centers of the windows (marked "C2" and "C3" in Fig. 12) to be an equal distance from all center points. For example, the distance from $0\,\text{m}$ (marked "C0" in Fig. 12(a) through (h)) to the first reflection center (marked "C1" in Fig. 12) equals the distance from the first reflection center to the second reflection center ("C2" in Fig. 12), which also equals the distance from the second reflection center to the third reflection center ("C3" in Fig. 12).
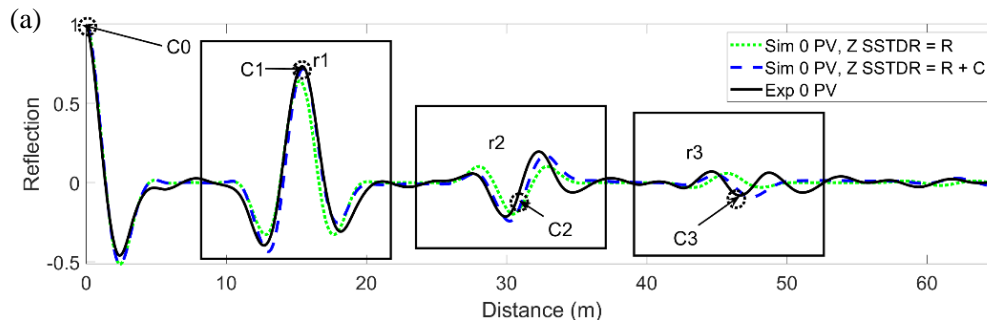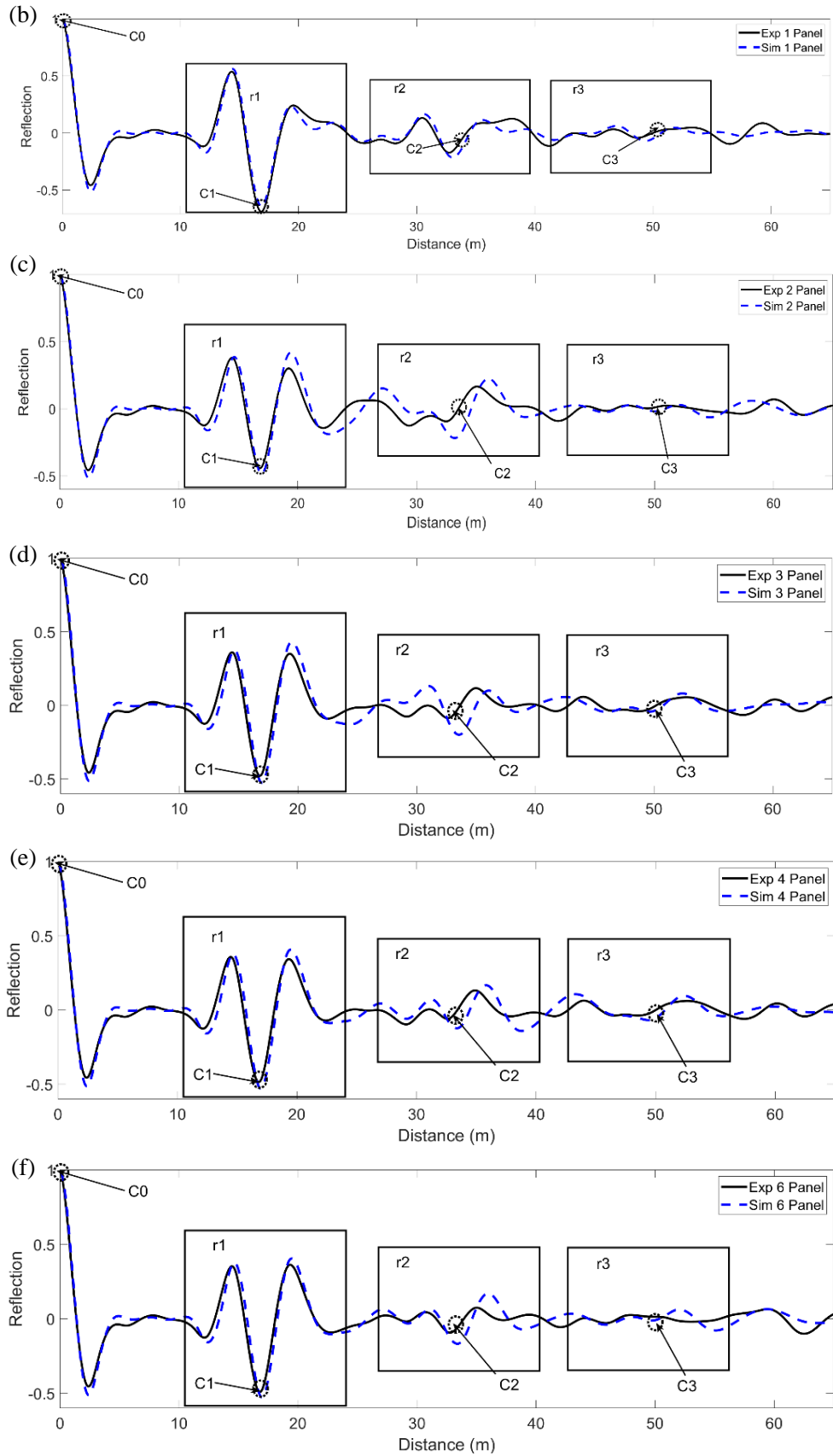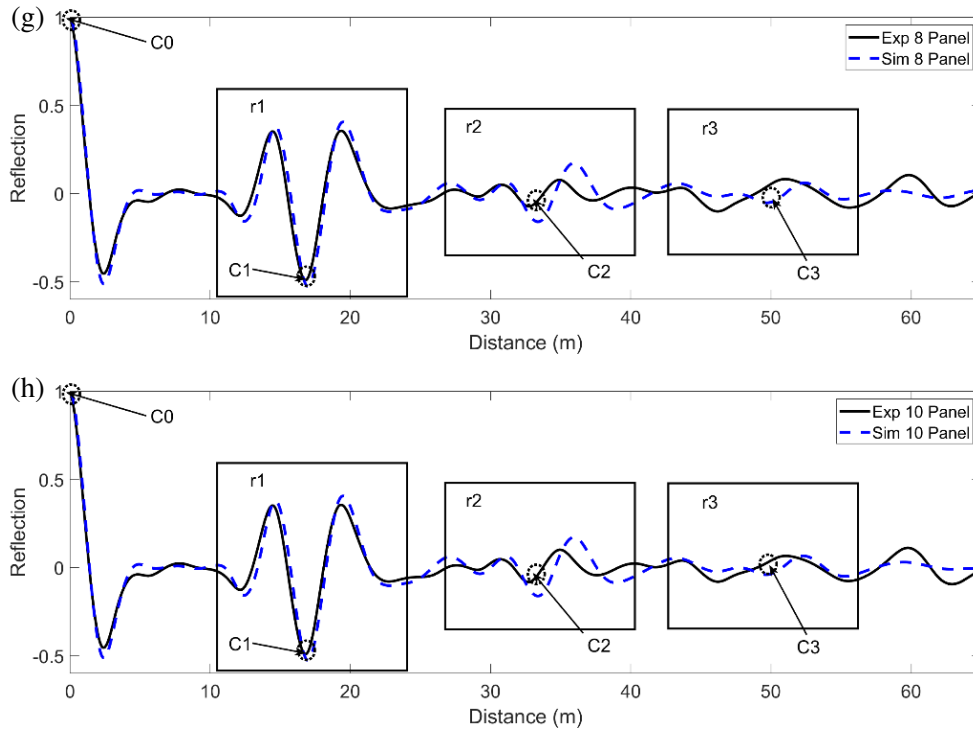
Figure 12. Experimental (solid) and simulated (dashed) SSTDR responses for PV modules connected in series. Plot (a), (b), (c), (d), (e), (f), (g), and (h) are 0 modules, 1 module, 2 modules, 3 modules, 4 modules, 6 modules, 8 modules, & 10 modules, respectively-0.

We chose three metrics to validate the simulations in the three time-gated windows. The first metric was the normalized correlation coefficient r, of the simulated and experimental data, defined as

$$r = \frac{\sum\limits_{i=1}^{N} x_{\text{sim}}(t_i) x_{\text{exp}}(t_i)}{\sqrt{\sum\limits_{i=1}^{N} |x_{\text{sim}}(t_i)|^2}\sqrt{\sum\limits_{i=1}^{N} |x_{\text{exp}}(t_i)|^2}} \tag{20}$$

where $x_{\text{sim}}(t)$ and $x_{\text{exp}}(t)$ represent the simulated and experimental data, respectively. The correlation coefficient measures how similar the shapes of the signals are and gives a value between -1 (representing the same shape but negated) and 1 (representing the same shape). The shape of the SSTDR response has been used to determine the amount of capacitance, and/or inductance associated with a load [11], so this metric is a good measure of how well the digital twin matches the impedance of the system. The second and third metrics are the percent errors of the peak amplitudes and locations associated with the reflection envelopes for both the simulated and experimental SSTDR data, respectively. In reflectometry, the reflection peak amplitudes measure both the amount of signal attenuation from a lossy transmission line and the ratio of a load resistance compared to the characteristic impedance of the transmission line [29]. The reflection peak locations are used to measure the physical distance to impedance discontinuities [4]. In our analysis, the reflection envelopes were determined using the envelope of the signal, computed from the absolute value of the analytic signal [21], of each time-gated window. The three metrics for all three reflections are calculated, and the results are given in Table 2.

From Table 2, the simulated first reflection for 0, 1, 2, 3, 4, 6, 8, and 10 PV modules connected in series matches well with experimental data in terms of all three metrics. The correlation coefficient is above 0.9; the percent error for the envelope peak location is less than 5%; and the percent error for the envelope peak amplitude is less than 10%. For the second reflection, the simulated SSTDR responses for 0, 1, 2, 4, 6, 8, and 10 (not 3) PV modules in series matches moderately well in terms of the correlation

Table 2. Validation results for simulated SSTDR data.

PPV	1st Reflection			2nd Reflection			3rd Reflection		
	Corr (c)	Err % Pk Loc.	Err Pk Amp.	Corr (c)	Err % Peak Loc.	Err % Pk Amp.	Corr (c)	Err % Peak Loc.	Err % Pk Amp.
0	0.98	1.48	1.01	0.87	0.00	7.66	0.29	2.70	5.39
1	0.98	2.08	5.09	0.83	1.70	24.80	0.35	16.93	29.46
2	0.94	3.42	8.37	0.53	1.32	35.43	0.28	0.0	15.27
3	0.95	0.66	10.06	0.02	3.63	53.70	0.76	9.62	26.48
4	0.96	0.66	8.86	0.52	6.19	31.97	0.84	25.0	82.51
6	0.96	0.0	6.73	0.47	4.44	98.94	0.42	0.0	8.32
8	0.97	0.0	6.81	0.37	0.66	131.0	0.38	27.9	45.1
10	0.96	0.0	6.77	0.47	0.32	79.47	0.68	28.35	51.35

coefficient and the envelope peak location, but not as well on the envelope peak amplitude. The error for the amplitude peaks could be improved by improving the model of the transmission line impedance, so the attenuation factor is more accurate. For the third reflection, the simulated SSTDR responses partially match experimental data in terms of the correlation coefficient for 0, 1, 2, 3, 4, 6, 8, and 10 PV modules connected in series. Based on these results, our digital twin simulations of SSTDR propagation through solar modules are reliable for the first and second reflections but not as accurate for the third SSTDR reflection.

5.2. Validation for Simulation of Partial Disconnects

We further validate our digital twin method by simulating SSTDR responses resulting from full open MC4 disconnections (illustrated in Fig. 3(c)) on the top lead located between each pair of modules in an experimental setup of 10 modules connected in series (locations marked with X_i in Fig. 13). The goal is to be able to identify where the MC4 disconnections are located from the simulated SSTDR responses. We will use the digital twin and an algorithm based on the peaks seen in the responses to determine the location of disconnections within this system. Other methods to do this include identifying the point at which the baselined X_i disconnection data diverged from the zero line data with approximately a 1% change [42], but we have chosen this method for its computational simplicity.
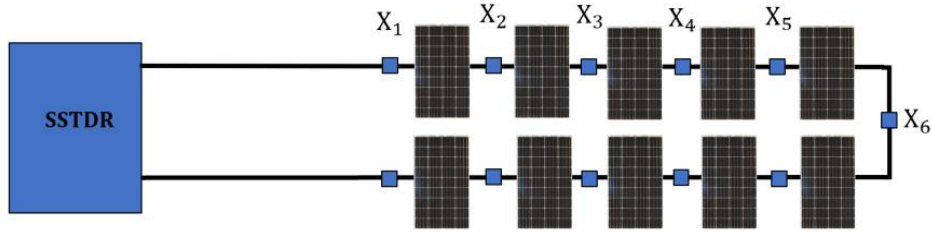
Figure 13. Experimental setup with 10 modules connected in series illustrating the MC4 disconnect locations marked X_i.

Before showing our simulations, it is useful to show the experimental SSTDR responses of the open circuit disconnections and then explain how one would interpret the data to locate each disconnection from experimental data. Fig. 14 shows the experimental MC4 disconnection data for each X_i MC4 connector, where $1 \leq i \leq 6$. Each X_i disconnection data was formulated by subtracting the baseline data (10 module setup with no disconnections) from the data associated with the experimental setup consisting of 10 modules connected in series and disconnecting the X_i MC4 connector for $1 \leq i \leq 6$.
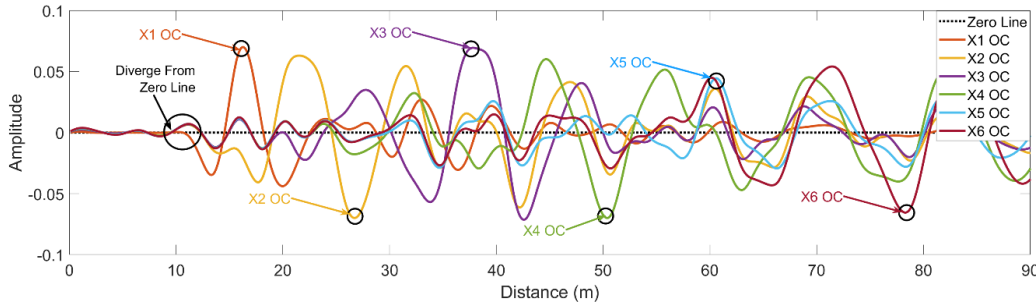
Figure 14. Experimental SSTDR responses for MC4 disconnections X_1 through X_6 showing the OC location alternating from maximum peak to minimum trough of data.

The first open circuit disconnection point X_1 located at $16\,\mathrm{m}$ is easily identified by the maximum. To observe all the X_i disconnection data at approximately the same amplitude, we scaled the X_1 data to be roughly the same amplitude as the remaining SSTDR responses. The disconnection points X_2, X_3, X_4, X_5, and X_6 are identified next. To locate open circuit faults, maximum peak locations are typically identified [4]. We interpret the open circuit locations differently here. For example, the point X_2 is identified as the minimum valued trough of the X_2 disconnection data, and X_3 point is identified as the maximum valued peak of the X_3 data. Hence, the X_i points for $1 \leq i \leq 6$ alternate from being the maximum valued peak to the minimum valued trough until the X_6 OC location is reached. It is important to also note that the effective distance between each X_i location and its neighboring Xi locations is approximately $11.47\,\mathrm{m}$, which is the measured effective length of a module and its connecting cables, as calculated in Section 3. To illustrate this more fully, Table 3 shows the location of each X_i using the measured effective distance, the corresponding maximum peaks and minimum troughs where we interpret the MC4 disconnection locations and the error percentage.

Table 3. Validation results for simulated SSTDR data.

MC4 OC Disconnection	Effective Distance Δd (m)	Experimental Data Peak or Trough Location (m)	Peak or Trough	Percent Error %
X_1	15.2	16.2	Peak	6.4
X_2	26.7	26.7	Trough	0.7
X_3	38.2	37.7	Peak	0.2
X_4	49.7	50.4	Trough	2.6
X_5	61.1	60.6	Peak	0.4
X_6	72.6	78.3	Trough	8.9

The justification for why we interpret the X_i points as alternating between the maximum peak and the minimum trough for an open circuit load is described by the effects of the PV module transmission coefficient $T_{\mathrm{PV}}(\omega)$ on the incident SSTDR signal $X(\omega)$ for each X_i SSTDR response. For the X_1 data, a simplified (neglecting multi-path reflections) SSTDR response $X_1'(\omega)$ is calculated as

$$X_1'(\omega) = X(\omega)\Gamma(\omega)_{\mathrm{OC1}} \tag{21}$$

where $\Gamma(\omega)_{\mathrm{OC1}}$ is the reflection coefficient for the first MC4 disconnection ($\Gamma_{\mathrm{MC4}}(\omega) = 1$). For the X_2 data, the SSTDR response is calculated as

$$X_2'(\omega) = X(\omega)\left[T_{\mathrm{PV}}(\omega)\right]^2 \Gamma(\omega)_{\mathrm{OC2}} \tag{22}$$

where $\Gamma(\omega)_{\mathrm{OC2}} = 1$. X_3 through X_6 responses are calculated as

$$X_3'(\omega) = X(\omega)\left[T_{\mathrm{PV}}(\omega)\right]^4 \Gamma(\omega)_{\mathrm{OC3}} \tag{23}$$

$$X_4'(\omega) = X(\omega)\left[T_{\text{PV}}(\omega)\right]^6 \Gamma(\omega)_{\text{OC4}} \tag{24}$$

$$X_5'(\omega) = X(\omega)\left[T_{\text{PV}}(\omega)\right]^8 \Gamma(\omega)_{\text{OC5}} \tag{25}$$

$$X_6'(\omega) = X(\omega)\left[T_{\text{PV}}(\omega)\right]^{10} \Gamma(\omega)_{\text{OC6}} \tag{26}$$

where $\Gamma(\omega)_{\text{OC}} = 1$. Note that for X_2, X_3, X_4, X_5, and X_6 responses, the transmission coefficient power doubles the number of module pairs because the signal travels through the modules and back to the SSTDR device.

The shape of the signal and whether the maximum magnitude of the data is a peak or a trough is largely affected by the transmission coefficient of the module. To illustrate how the transmission coefficient powers affect the incident SSTDR signal, we have plotted the inverse Fourier transform of each $X_i'(\omega)$ in Fig. 15. The squared transmission coefficient introduces an overall phase shift of 180 degrees, which flips the signal from a maximum valued peak to a minimum valued trough. This implies that a single transmission coefficient performs a 90 degree shift on the data. For the data in Fig. 15, the exact positions of the peaks are not important. We show this data to solely show that SSTDR responses are flipping as the SSTDR signal propagates through a PV module.
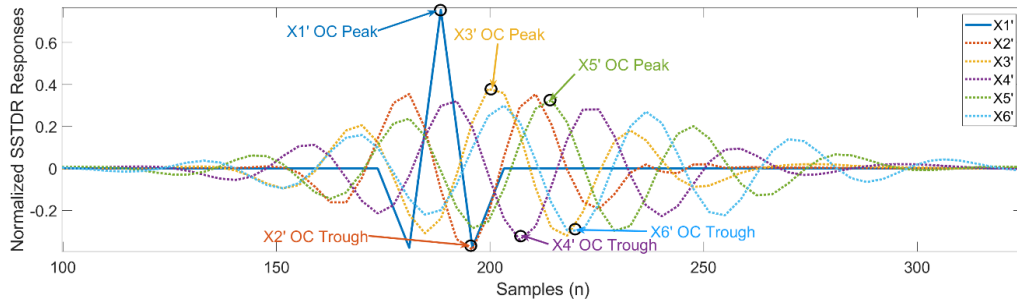
Figure 15. Simplified simulated X_1 through X_6 responses to illustrate the effect of $T_{\text{PV}}(\omega)$ in flipping the response.

We used the experimentally extracted transmission coefficient of the module $T_{\text{PV}}(\omega)$ described in Section 3 to see all the maximum magnitude peaks and troughs for the X_i responses on the same plot, and we have normalized each data set by being divided by L2 norm of itself as

$$X_i(\omega) = \frac{X_i(\omega)}{\sum\limits_{q=1}^{Q} |X_i(\omega_q)|^2} \tag{27}$$

for Q different frequencies. Each of the i data sets in Fig. 15 has also been shifted to the right so that each i data set has a spacing of 2 samples from the $i-1$ and $i+1$ data set so that we can distinguish the data set's point of maximum magnitude (whether it is a peak or trough). Without this manual shift in the data, all the maximum magnitude peaks and troughs would be at the same location, making it difficult to distinguish between the respective data sets. Therefore, because of the transmission coefficient, the open circuit response that would normally have a maximum magnitude peak can be flipped up-side-down to be a minimum valued trough, similar to a traditional short circuit load response [33].

The simulated SSTDR responses of the corresponding X_1, X_2, X_3, X_4, X_5, and X_6 after baseline subtraction are shown in Fig. 16. The simulations show a similar alternating sign pattern to the experimental data.

The metric to validate our simulated SSTDR disconnection responses is the percent error between simulated and experimental data open circuit locations. The simulated and experimental open circuit locations and the percent error are listed in Table 4. All the simulated disconnect locations, except for X_4, have an error of less than 5%. Although the expected minimum valued trough location of the X_4 data has an 18.5% error, we note that the second least minimum valued trough, which we denote as X_4' in Fig. 16, is located at 49.79 m and has an error of 1.2 %. We also note that the error in the X_4 OC
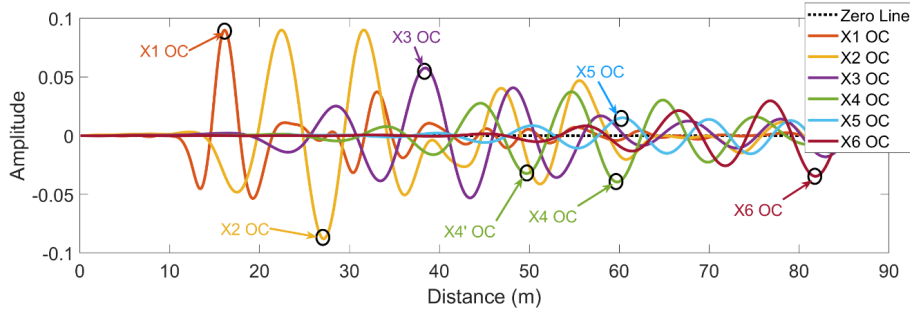
Figure 16. Simplified simulated X_1 through X_6 responses to illustrate the effect of $T_{\mathrm{PV}}(\omega)$ in flipping the response.

location is likely not because of differences in the PV modules. In [43], the variability in SSTDR data was quantified for various parameters, e.g., switching out PV modules. It was found that the greatest change was in the reflection coefficient amplitude not in peak location. Thus, the ordering of the specific PV modules would not affect the open circuit locations with as much error that is shown in Table 4.

Table 4. Results for simulated vs experimental MC4 disconnection distance to trough with greatest magnitude.

Sim MC4 OC Disconnection	Sim Data (m)	Exp Data (m)	Error Exp vs Sim (%)
X_1	16.1	16.2	0.6
X_2	27.2	26.7	1.9
X_3	38.4	37.7	1.9
X_4	59.7	50.4	18.5
X_5	60.4	60.6	0.3
X_6	81.9	78.3	4.6

Overall, we have measured how well we can simulate SSTDR propagation through N connected modules in series and compared the first three major reflections and have measured how well we can simulate open circuit SSTDR responses.

6. CONCLUSION

We developed a method to extract accurate model parameters from experimental SSTDR data to produce a digital twin SSTDR response that can be used for fault detection and classification in PV systems. The novelty of this paper is our procedure for calculating frequency-dependent model parameters for accurate modeling, our adapted fast graph simulation engine for complex multi-dimensional PV systems, and our demonstration that these systems can accurately predict fault behavior in PV systems. This modeling method could produce an accurate SSTDR response. Using the extracted model parameters, we chose to use a computationally efficient graph network engine to produce the digital twin SSTDR responses, although the model parameters we extracted could be used in any reflectometry modeling method. We demonstrated the accuracy of the model parameters to simulate the SSTDR responses for $P = 0$ to $P = 10$ PV modules connected in series compared to experimental data. The modules are connected in pairs so that for every module connected on the top lead, there is also one on the bottom lead (as per Fig. 1). An odd number of modules are still connected by having a single module on the end where both the top and bottom leads join (Fig. 1). The simulated data matched well with the experimental data for the first two reflections. In addition, we were able

to simulate open circuit disconnections at the MC4 locations in a PV system with 10 PV modules connected in series. All but one disconnect location had an error of less than 5% compared to the corresponding experimental disconnection locations.

To improve the simulations, one could explore using optimization and regression models to improve each model parameter. One could use different modulation frequencies for the SSTDR signal. This paper focused on simulations for 24 MHz modulated SSTDR simulations. One could also apply regression to fit frequency dependent reflection and transmission coefficients in the graph network.

ACKNOWLEDGMENT

DISCLOSURE

Dr. Furse is a co-founder of Livewire Innovation, Inc. which is commercializing SSTDR technology, and therefore has a financial conflict of interest with this company.

REFERENCES

1. Abdul Mawjood, K., S. S. Refaat, and W. G. Morsi, "Detection and prediction of faults in photovoltaic arrays: A review," *2018 IEEE 12th International Conference on Compatibility, Power Electronics and Power Engineering (CPE-POWERENG 2018)*, 1–8, Apr. 2018, doi: 10.1109/CPE.2018.8372609.

2. Alam, M. K., F. Khan, J. Johnson, and J. Flicker, "A comprehensive review of catastrophic faults in PV arrays: Types, detection, and mitigation techniques," *IEEE Journal of Photovoltaics*, Vol. 5, No. 3, 982–997, May 2015, doi: 10.1109/JPHOTOV.2015.2397599.

3. Khalil, I. U., et al., "Comparative analysis of photovoltaic faults and performance evaluation of its detection techniques," *IEEE Access*, Vol. 8, 26676–26700, 2020, doi: 10.1109/ACCESS.2020.2970531.

4. Smith, P., C. Furse, and J. Gunther, "Analysis of spread spectrum time domain reflectometry for wire fault location," *IEEE Sensors Journal*, Vol. 5, No. 6, 1469–1478, 2005.

5. Jones, S. B., J. M. Wraith, and D. Or, "Time domain reflectometry measurement principles and applications," *Hydrological Processes*, Vol. 16, No. 1, 141–153, 2002.

6. Minet, J., S. Lambot, G. Delaide, J. A. Huisman, H. Vereecken, and M. Vanclooster, "A generalized frequency domain reflectometry modeling technique for soil electrical properties determination," *Vadose Zone Journal*, Vol. 9, No. 4, 1063–1072, 2010.

7. Shin, Y.-J., et al., "Application of time-frequency domain reflectometry for detection and localization of a fault on a coaxial cable," *IEEE Transactions on Instrumentation and Measurement*, Vol. 54, No. 6, 2493–2500, 2005.

8. Lo, C. and C. Furse, "Noise domain reflectometry for wire fault location," *IEEE Trans. EMC*, Vol. 47, No. 1, 97–104, 2005.

9. Furse, C. M., M. Kafal, R. Razzaghi, and Y.-J. Shin, "Fault diagnosis for electrical systems and power networks: A review," *IEEE Sensors Journal*, Vol. 21, No. 2, 888–906, Jan. 2021, doi: 10.1109/JSEN.2020.2987321.

10. Furse, C., Y. C. Chung, C. Lo, and P. Pendayala, "A critical comparison of reflectometry methods for location of wiring faults," *Smart Structures and Systems*, Vol. 2, No. 1, 25–46, 2006.

11. Benoit, E., et al., "Applicability of SSTDR analysis of complex loads," *2019 IEEE International Symposium on Antennas and Propagation and USNC-URSI Radio Science Meeting*, 2087–2088, 2019, doi: 10.1109/APUSNCURSINRSM.2019.8888841.

12. Smaïl, M.-K., T. Hacib, L. Pichon, and F. Loete, "Detection and location of defects in wiring networks using time-domain reflectometry and neural networks," *IEEE Transactions on Magnetics*, Vol. 47, No. 5, 1502–1505, 2011.

13. Smail, M. K., H. R. E. H. Bouchekara, L. Pichon, H. Boudjefdjouf, and R. Mehasni, "Diagnosis of wiring networks using particle swarm optimization and genetic algorithms," *Computers & Electrical Engineering*, Vol. 40, No. 7, 2236–2245, 2014, doi: https://doi.org/10.1016/j.compeleceng.2014.07.002.

14. Boudjefdjouf, H., R. Mehasni, A. Orlandi, H. R. E. H. Bouchekara, F. de Paulis, and M. K. Smail, "Diagnosis of multiple wiring faults using time-domain reflectometry and teaching-learning-based optimization," *Electromagnetics*, Vol. 35, No. 1, 10–24, 2015, doi: 10.1080/02726343.2015.971659.

15. Zhang, Q., M. Sorine, and M. Admane, "Inverse scattering for soft fault diagnosis in electric transmission lines," *IEEE Transactions on Antennas and Propagation*, Vol. 59, No. 1, 141–148, Jan. 2011, doi: 10.1109/TAP.2010.2090462.

16. Kingston, S. R., et al., "Measurement of capacitance using spread spectrum time domain reflectometry (SSTDR) and dictionary matching," *IEEE Sensors Journal*, Vol. 20, No. 17, 10102–10109, 2020.

17. Edun, A. S., et al., "Finding faults in PV systems: Supervised and unsupervised dictionary learning with SSTDR," *IEEE Sensors Journal*, 2020.

18. Roy, S., M. K. Alam, F. Khan, J. Johnson, and J. Flicker, "An irradiance-independent, robust ground-fault detection scheme for PV arrays based on spread spectrum time-domain reflectometry (SSTDR)," *IEEE Transactions on Power Electronics*, Vol. 33, No. 8, 7046–7057, 2017.

19. Ye, C., et al., "A digital twin of bridges for structural health monitoring," *Proceedings of the 12th International Workshop on Structural Health Monitoring*, 2019.

20. Seshadri, B. R. and T. Krishnamurthy, "Structural health management of damaged aircraft structures using digital twin concept," *25th AIAA/AHS Adaptive Structures Conference*, 1675, 2017.

21. Ellis, H. D., et al., "A model for SSTDR signal propagation through photovoltaic strings," *IEEE Journal of Photovoltaics*, Vol. 10, No. 6, 1846–1852, 2020, doi: 10.1109/JPHOTOV.2020.3023801.

22. Tao, F., H. Zhang, A. Liu, and A. Y. C. Nee, "Digital twin in industry: State-of-the-art," *IEEE Transactions on Industrial Informatics*, Vol. 15, No. 4, 2405–2415, 2019, doi: 10.1109/TII.2018.2873186.

23. Nievinski, F. G. and K. M. Larson, "Forward modeling of GPS multipath for near-surface reflectometry and positioning applications," *GPS Solutions*, Vol. 18, No. 2, 309–322, 2014.

24. Regalado, C., R. M. Carpena, A. Socorro, and J. H. Moreno, "Time domain reflectometry models as a tool to understand the dielectric response of volcanic soils," *Geoderma*, Vol. 117, Nos. 3–4, 313–330, 2003.

25. Keysight Technologies, "Vector network analyzer data sheet," Keysight Technologies. [Online]. Available: https://www.keysight.com/us/en/assets/7018-01424/data-sheets/5989-5479.pdf.

26. Kingston, S., et al., "A SSTDR methodology, implementations, and challenges," *Sensors*, Vol. 21, No. 16, 2021, doi: 10.3390/s21165268.

27. Kingston, S. R., et al., "Spread spectrum time domain reflectometry and steepest descent inversion to measure complex impedance," *Applied Computational Electromagnetics Society Journal*, Vol. 36, No. 2, 2021.

28. Harley, J. B., M. U. Saleh, S. Kingston, M. A. Scarpulla, and C. Furse, "Fast transient simulations for multi-segment transmission lines with a graphical model," *Progress In Electromagnetics Research*, Vol. 165, 67–82, 2019.

29. Ulaby, F., E. Michielssen, and U. Ravaioli, *Fundamentals of Applied Electromagnetics*, 6th Edition, Prentice Hall, 2010.

30. Furse, C., et al., "Spread spectrum time domain reflectometry for complex impedances: Application to PV arrays," *2018 IEEE AUTOTESTCON*, 1–4, Sep. 2018, doi: 10.1109/AUTEST.2018.8532521.

31. Saleh, M. U., et al., "Signal propagation through piecewise transmission lines for interpretation of reflectometry in photovoltaic systems," *IEEE Journal of Photovoltaics*, Vol. 9, No. 2, 506–512, 2018.

32. "Live cable fault detection by LiveWire innovation," LiveWire Innovation. [Online]. Available: https://www.livewireinnovation.com/.

33. Jayakumar, N. K. T., et al., "Postprocessing for improved accuracy and resolution of spread spectrum time-domain reflectometry," *IEEE Sensors Letters*, Vol. 3, No. 6, 1–4, 2019, doi: 10.1109/LSENS.2019.2916636.

34. Wadell, B. C., *Transmission Line Design Handbook*, Artech House, The Artech House Microwave Library, Boston, 1991.

35. Edun, A. S., N. K. T. Jayakumar, S. R. Kingston, C. M. Furse, M. A. Scarpulla, and J. B. Harley, "Spread spectrum time domain reflectometry with lumped elements on asymmetric transmission lines," *IEEE Sensors Journal*, Vol. 21, No. 2, 921–929, 2020.

36. Kim, K. A., C. Xu, L. Jin, and P. T. Krein, "A dynamic photovoltaic model incorporating capacitive and reverse-bias characteristics," *IEEE Journal of Photovoltaics*, Vol. 3, No. 4, 1334–1341, 2013, doi: 10.1109/JPHOTOV.2013.2276483.

37. "Peimar Group SG300M |Reviews and Ratings |EnergySage," [Online]. Available: https://www.energysage.com/panels/Peimar+Group/SG300M/.

38. Ferrara, C. and D. Philipp, "Why Do PV modules fail?," *Energy Procedia*, Vol. 15, 379–387, 2012, doi: https://doi.org/10.1016/j.egypro.2012.02.046.

39. Moffitt, J. R., C. Osseforth, and J. Michaelis, "Time-gating improves the spatial resolution of STED microscopy," *Opt. Express*, Vol. 19, No. 5, 4242–4254, Feb. 2011, doi: 10.1364/OE.19.004242.

40. Weedon, W. H. and C. M. Rappaport, "A general method for FDTD modeling of wave propagation in arbitrary frequency-dispersive media," *IEEE Transactions on Antennas and Propagation*, Vol. 45, No. 3, 401–410, 1997.

41. Furse, C. M., J.-Y. Chen, and O. P. Gandhi, "The use of the frequency-dependent finite-difference time-domain method for induced current and SAR calculations for a heterogeneous model of the human body," *IEEE Transactions on Electromagnetic Compatibility*, Vol. 36, No. 2, 128–133, 1994.

42. Saleh, M. U., et al., "Detection and localization of damaged photovoltaic cells and modules using spread spectrum time domain reflectometry," *IEEE Journal of Photovoltaics*, Vol. 11, No. 1, 195–201, Jan. 2021, doi: 10.1109/JPHOTOV.2020.3030185.

43. Benoit, E., et al., "Quantifying the window of uncertainty for SSTDR measurements of a photovoltaic system," *IEEE Sensors Journal*, Vol. 21, No. 8, 9890–9899, 2021, doi: 10.1109/JSEN.2021.3059412.